Research Square

Preprints are preliminary reports that have not undergone peer review.
They should not be considered conclusive, used to inform clinical practice,
or referenced by the media as validated information.

Comparative Evaluation of EN-1561-GJL-300 and EN-16079-GJV-300 Cast Irons Using Process and Finite-Element Simulations versus Experimental Tensile and Microstructural Data for Engine-Material Quality

Cem ULUC

cemuluc@hotmail.com

Gazi University

Hasan HASIRCI

Gazi University

Research Article

Keywords: compacted graphite iron, flake graphite iron, control-volume simulation, finite-element analysis, Johnson–Cook model, cooling curve, graphite morphology, engine block material

Posted Date: November 16th, 2026

DOI: https://doi.org/10.21203/rs.3.rs-11233682/v1

License: This work is licensed under a Creative Commons Attribution 4.0 International License.
Read Full License

Additional Declarations: No competing interests reported.

Comparative Evaluation of EN-1561-GJL-300 and EN-16079-GJV-300 Cast Irons Using Process and Finite-Element Simulations versus Experimental Tensile and Microstructural Data for Engine-Material Quality

Cem ULUC[1], Hasan HASIRCI[2]

1. Graduate School Of Natural And Applied Sciences, Metallurgical and Materials Engineering, Gazi University, Ankara, Türkiye.
2. Technology Faculty, Metallurgical and Materials Engineering, Gazi University, Ankara, Türkiye.

*Corresponding author(s). E-mail(s): cemuluc@hotmail.com ; cem.uluc@gazi.edu.tr
Contributing authors: hasirci@gazi.edu.tr ;
†These authors contributed equally to this work.

Abstract

This study compares the tensile properties and microstructural constituents of EN-1561-GJL-300 (lamellar graphite iron) and EN-16079-GJV-300 (compacted/vermicular graphite iron) on the basis of experimental tensile testing. metallographic analysis. control-volume casting-process simulation. and finite-element tensile-test simulation. Cast Y-block specimens were produced in furan-bound sand moulds at 1400–1410 °C from two separate melts. Tensile tests were carried out in accordance with EN 1561 and EN 16079 on a minimum of ten specimens per material at a crosshead speed of 1 mm·min^{-1}. Brinell hardness was measured at ten locations on each specimen (3000 kgf. 10 mm steel ball). and microstructure was quantified on at least 15 fields of view per condition. both as-polished (graphite morphology) and after 2% nital etching (matrix phases). The experimental melt for GJL-300 exhibited a tensile strength of 256 MPa. predominantly Type-A flake-graphite morphology (≥90% of evaluated fields). 15 vol.% graphite. an elongated graphite length fraction of 45%. and a matrix of approximately 71% pearlite / 29% ferrite. The experimental melt for GJV-300 exhibited a tensile strength of 313 MPa. 8% nodularity (ASTM A247) . 12 vol.% graphite. and a matrix of approximately 89% pearlite / 11% ferrite. For EN-16079-GJV-300, the deviations between the experimental results and the CV and FE simulations were 35.8% and 7.0%, respectively. For EN-1561-GJL-300, the corresponding deviations were 30.9% and 6.6%, respectively. The markedly smaller deviation of the FE results is attributable to the use of the actual tensile-specimen geometry and identical boundary conditions rather than the as-cast Y-block cross-section employed in the CV workflow. Cooling-curve analysis indicates full solidification at approximately 250 s for GJL-300 (with a graphitisation interval of about 180 s) and approximately 184 s for GJV-300 (graphitisation interval of about 88 s). consistent with the measured higher graphite volume fraction and longer flake length of the GJL-300 melt.

The proposed combined workflow provides a validated methodology for selecting engine-block materials by integrating casting-process simulation, finite-element analysis, and experimental characterization.

Keywords: compacted graphite iron; flake graphite iron; control-volume simulation; finite-element analysis; Johnson–Cook model; cooling curve; graphite morphology; engine block material

1. Introduction

Critical components of internal-combustion engines such as cylinder blocks and cylinder heads must simultaneously satisfy high mechanical strength. good thermal conductivity. vibration-damping capacity. and thermomechanical fatigue resistance. Lamellar graphite cast irons of the EN-GJL family have traditionally been preferred for engine-block production because of their good machinability and high damping capacity. However. rising peak firing pressures and tightening emissions legislation impose higher strength and stiffness requirements [1] Numerical modelling of solidification behaviour is therefore critical for the prior prediction of mechanical performance. and advances in casting-process simulation and structural-analysis simulation are essential to meet this need [1].

The mechanical properties of EN-1561-GJL-300 depend strongly on graphite morphology. flake length. matrix-phase distribution (ferrite/pearlite ratio). and eutectic-cell structure [1]. Recent experimental work has shown that temperature and strain rate significantly influence the tensile behaviour of GJL-grade cast irons and that heat treatment can modify the microstructure and mechanical properties of EN-1561-GJL-300 through phase transformations [1]. In vermicular graphite cast irons. the effects of austempering parameters on tensile and yield strength have been modelled using regression and response-surface methodology with high coefficients of determination [2]. These observations emphasise the importance of analysing material behaviour under conditions that are representative of in-service loading.

Compacted graphite irons offer lower stress concentrations and higher tensile strength than lamellar graphite irons because of their worm-like graphite morphology. The elastic modulus and fatigue strength of CGI are markedly higher than those of EN-GJL-class irons [3] Post-2015 microstructure-based modelling studies have shown that numerical quantification of graphite morphology from real micrographs enables more accurate prediction of mechanical behaviour [4,5]. The localised microstructural variations that develop during solidification must be incorporated directly into FE-based stress–strain analyses. since local mechanical behaviour differs from predictions based on a homogeneous-material assumption [6]. In CGI used for engine blocks. narrow process windows make precise control of graphite morphology essential. Solidification time. inoculation amount. fading time. local cooling rate. and feeding conditions directly affect the microstructural quantities that govern tensile and fatigue behaviour [7]. Treating the heat-transfer coefficient as a function of mould height is important for accurate prediction of centreline porosity [8].

These findings demonstrate that casting-simulation results must be evaluated jointly with mechanical tests. Casting-simulation software can predict mechanical properties from process parameters such as solidification behaviour and defect formation. but the heterogeneous nature of the microstructure inevitably introduces deviations. Recent work has shown that more sophisticated modelling strategies—going beyond purely deterministic approaches—can improve result reliability [9]. and that optimisation of mould design through simulation produces tensile-test results that agree closely with numerical predictions [10]. The finite-element method is widely used for the numerical simulation of mechanical tests. and accurate simulation of tensile-test geometry and boundary conditions reproduces experimental results with high fidelity [11]. Incorporating graphite morphology directly into microstructure-based damage models improves the accuracy of crack initiation and propagation predictions in CGI [5]. Joint modelling of local mechanical behaviour and residual stresses significantly alters results in the post-yield regime [6]. Recent work emphasises that engine-material selection should consider thermomechanical fatigue. temperature-dependent deformation. and

machinability—not only tensile strength—[12,13]. A comparative evaluation of EN-1561-GJL-300 and EN-16079-GJV-300 across both mechanical and microstructural metrics is therefore essential for engine applications. This comprehensive comparison underscores the necessity of integrating locally varying mechanical properties—arising from geometry, chemical composition, and cooling rates—into standard structural analyses for automotive components[14] Furthermore, such integrated approaches enable the refinement of casting-process parameters to manage the inherent uncertainties caused by thermal gradients and section-thickness variations [14,17] Specifically, leveraging virtual casting simulations to incorporate process variability facilitates the probabilistic modeling of expected local properties, thereby assisting designers in achieving robust and reliable component development. By integrating these high-fidelity material models into the design phase, engineers can mitigate the risks associated with manufacturing non-optimal components that might otherwise suffer from unexpected in-use failures [6,9] Moreover, the adoption of multiscale modeling frameworks, which account for both graphite anisotropy and local matrix phase constituents, provides a more granular understanding of the material's structural integrity[18] This multiscale approach, combined with cohesive zone modeling, allows for the precise simulation of interfacial debonding and brittle fracture phenomena, which are critical for characterizing failure in both gray and vermicular graphite iron morphologies.

In the literature. systematic comparative studies that simultaneously combine experimental testing. casting-process simulation. and FE tensile-test simulation of EN-1561-GJL-300 and EN-16079-GJV-300 are limited. In particular. the joint evaluation of control-volume solidification analyses and tensile-test results with explicit quantification of the resulting deviations is rare. The present study addresses this gap. The main contributions of this study are:

(i) To the authors' knowledge, this is the first study of control-volume casting simulation and finite-element tensile simulation for EN-GJL-300 and EN-GJV-300,

(ii) quantitative validation of both simulation approaches using tensile tests and microstructural characterization,

(iii) evaluation of the influence of specimen geometry on tensile-strength prediction accuracy,

(iv) assessment of graphite morphology and matrix-phase prediction capability for engine-material selection.

2. Experimental

2.1 Material. Casting and Specimen Preparation

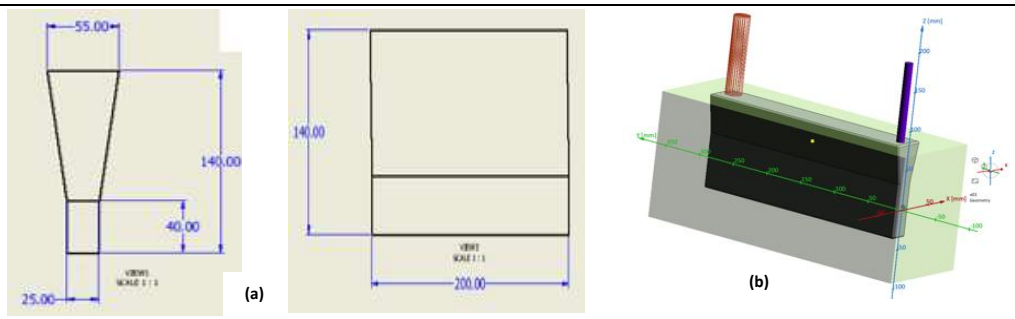
Melting was performed in a medium-frequency induction furnace. Two separate melts were produced and poured into furan-bonded sand moulds to obtain the EN-1561-GJL-300 and EN-16079-GJV-300 compositions. Pouring temperatures were in the range 1400–1410 °C. using standard Y-block moulds of which the technical drawing and a three-dimensional representation are shown in Figure 1. Chemical analyses were carried out with an OBLF optical-emission spectrometer.

Table 1. Chemical composition of EN-1561-GJL-300 (wt.%)

Melt	C	Si	Mn	P	S	Cr	Ni	Al	Cu	Ti	Sn
1	3.20–3.30	1.85–2.00	0.40–0.80	<0.10	0.05–0.12	<0.25	<0.30	<0.03	0.60–0.70	max 0.02	0.08–0.09

Table 2. Chemical composition of EN-16079-GJV-300 (wt.%)

Melt	C	Si	Mn	P	S	Cr	Ni	Al	Cu	Ti	Sn
1	3.55–3.75	2.40–2.70	<0.30	<0.08	<0.02	<0.10	<0.30	<0.03	0.20–0.27	<0.25	<0.02



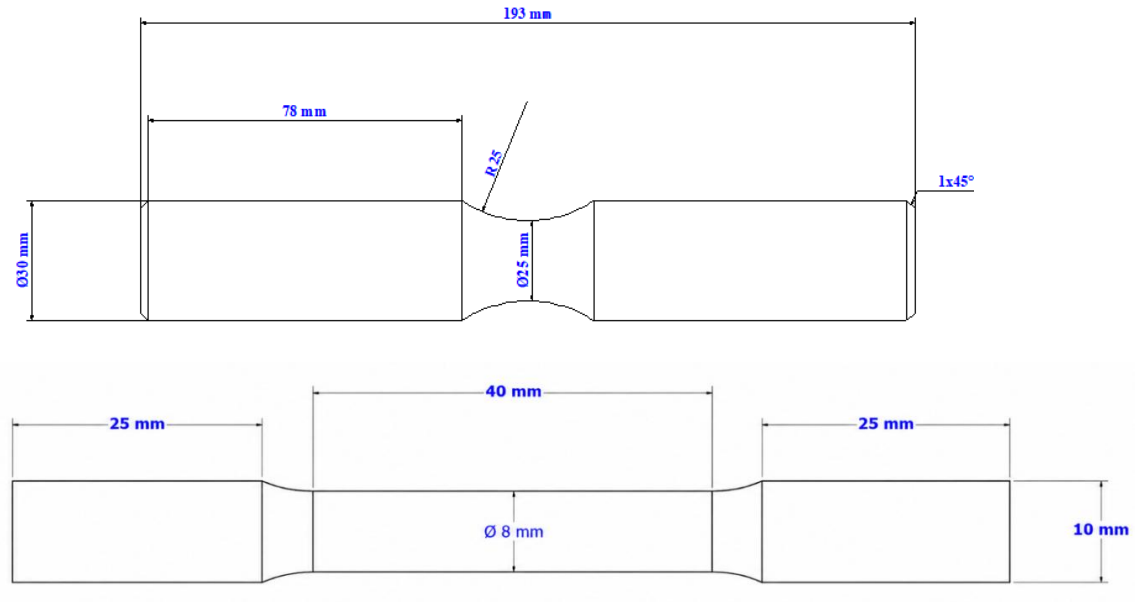
[Figure 1. Y-block specimens used in this study: (a) side and front technical drawing; (b) three-dimensional representation of the mould and the cast specimen]

2.2 Microstructural Analysis

Metallographic examination was performed to characterise the graphite morphology and the matrix-phase distribution. Specimens of 20 × 20 × 20 mm were sectioned from the Y-blocks with an ATM Brillant 300 cutting machine. hot-mounted in an ATM Opal 460. and ground and polished with an ATM Safire 350. The surface preparation sequence used 220–3000 mesh Al_2O_3 grinding papers followed by diamond polishing suspensions of 6. 3. and 1 µm. Graphite morphology was evaluated on the as-polished surface. and matrix phases were characterised after etching with 2% nital (HNO_3 in ethanol).

2.3 Hardness and Tensile Testing

Brinell hardness was measured on a BMS OBPC device using a 10 mm steel ball and a 3000 kgf load. with ten indentations per specimen. In accordance with EN 1561. tensile tests were performed on an Instron 3369 at a crosshead speed of 1 mm·min^{-1} with a minimum of ten test repetitions per material condition. on specimens shown in Figure 2.



[Figure 2. Tensile specimens in accordance with DIN EN 1561- DIN EN 1563]

2.4 Simulation Analysis

Two simulation workflows were used to compare with experimental tensile and microstructural data:

(i) a control-volume casting-process simulation. replicating the thermo-physical behaviour of the casting; and

(ii) a finite-element tensile-test simulation of the actual tensile-specimen geometry.

Geometry. mould material. pouring temperature. cooling conditions. inoculation type and amount. and chemical composition were matched to the experimental conditions. A digital twin of the tensile specimen was meshed at 0.5 mm element size.

The elasto-viscoplastic Johnson–Cook constitutive model was used to represent both materials in the FE simulation:

$$\sigma_y = \left(A + B_{\varepsilon}^{-p^n}\right)(1 + C \ln \dot{\varepsilon}^*)\left(1 - T^{*^m}\right)$$

where A is the reference yield stress. B is the strain-hardening modulus. n is the strain-hardening exponent. C is the strain-rate sensitivity coefficient. is the equivalent plastic strain. *is the dimensionless strain rate. and* } is the homologous temperature. Because grey cast irons exhibit asymmetric thermo-mechanical behaviour in tension and compression. separate J-C parameter sets for the tensile and compressive regimes were used. an approach which previous work has shown improves model fidelity. The Johnson–Cook constitutive model was selected because it simultaneously accounts for strain hardening, strain-rate sensitivity, and temperature-dependent material behaviour while remaining computationally efficient for engineering-scale finite-element simulations. This enables realistic reproduction of the tensile-test conditions and facilitates direct comparison between numerical predictions and experimental results. Previous studies have demonstrated that separate tensile and compressive Johnson–Cook parameter sets significantly improve the prediction accuracy for gray cast irons exhibiting asymmetric

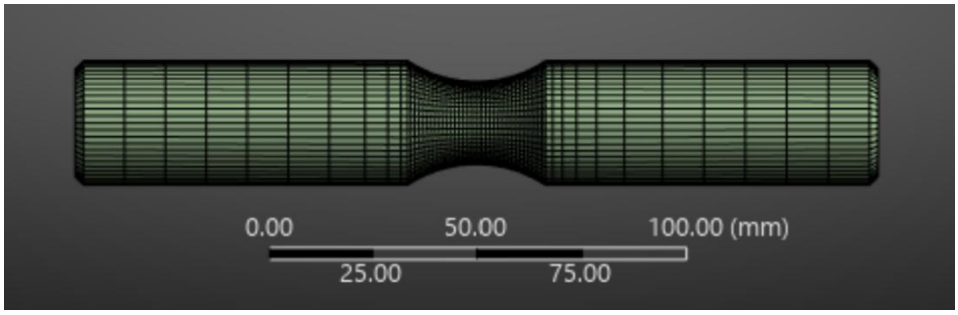
mechanical behaviour [15]. Mesh size was 0.5 mm (≈68.000 nodes); boundary conditions replicated the experimental test set-up (1 mm·min^{-1} displacement on the upper grip. fully fixed lower grip. room temperature).

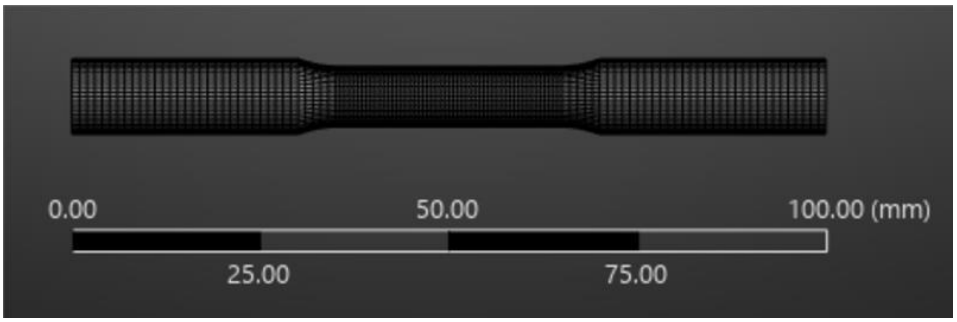
Table 3. Mechanical-property inputs used in the tensile-test FE simulation

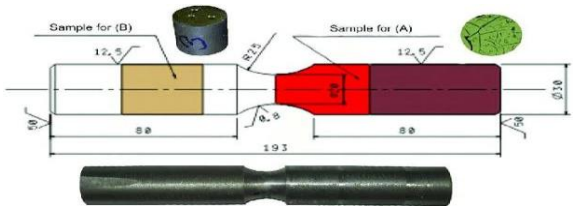
Material parameter	**EN-16079-GJV-300**	**EN-1561-GJL-300**
Ultimate tensile strength.	300–450 MPa	250–310 MPa
Young's modulus	140–157 GPa	90–115 GPa
Poisson's ratio	0.26–0.28	0.24–0.27
Yield strength.	210–415 MPa	175–225 MPa
Melting temperature.	1538 °C	1538 °C
Elongation.	%1.0–%2.5	%0.3–%1.0

Parameter	**EN-GJL-300 (T / C)**	**EN-GJV-300 (T / C)**
A [MPa]	195 / ~280	220 / ~310
B [MPa]	~320 / ~450	~380 / ~530
n [–]	0.26 / 0.36	0.32 / 0.42
C [–]	0.014 / 0.008	0.016 / 0.010
m [–]	1.03 / 1.03	0.90 / 0.90

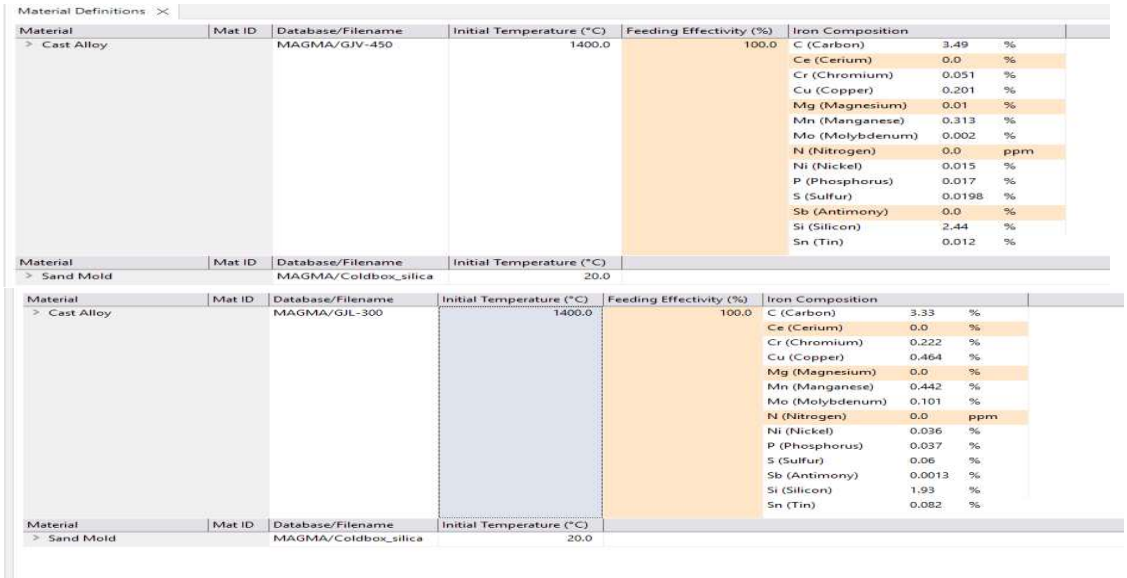
Note: The symbol "~" indicates calibrated values rather than directly measured material properties. These values were determined by inverse calibration based on the experimental tensile response using the methodology proposed by Özcan et al. [15].







[Figure 3. Finite-element tensile-test model for GJL-300 and GJV-300]



Material Definitions

Material	Mat ID	Database/Filename	Initial Temperature (°C)	Feeding Effectivity (%)	Iron Composition		
> Cast Alloy		MAGMA/GJV-450	1400.0	100.0	C (Carbon)	3.49	%
					Ce (Cerium)	0.0	%
					Cr (Chromium)	0.051	%
					Cu (Copper)	0.201	%
					Mg (Magnesium)	0.01	%
					Mn (Manganese)	0.313	%
					Mo (Molybdenum)	0.002	%
					N (Nitrogen)	0.0	ppm
					Ni (Nickel)	0.015	%
					P (Phosphorus)	0.017	%
					S (Sulfur)	0.0198	%
					Sb (Antimony)	0.0	%
					Si (Silicon)	2.44	%
					Sn (Tin)	0.012	%

Material	Mat ID	Database/Filename	Initial Temperature (°C)
> Sand Mold		MAGMA/Coldbox_silica	20.0

Material	Mat ID	Database/Filename	Initial Temperature (°C)	Feeding Effectivity (%)	Iron Composition		
> Cast Alloy		MAGMA/GJL-300	1400.0	100.0	C (Carbon)	3.33	%
					Ce (Cerium)	0.0	%
					Cr (Chromium)	0.222	%
					Cu (Copper)	0.464	%
					Mg (Magnesium)	0.0	%
					Mn (Manganese)	0.442	%
					Mo (Molybdenum)	0.101	%
					N (Nitrogen)	0.0	ppm
					Ni (Nickel)	0.036	%
					P (Phosphorus)	0.037	%
					S (Sulfur)	0.06	%
					Sb (Antimony)	0.0013	%
					Si (Silicon)	1.93	%
					Sn (Tin)	0.082	%

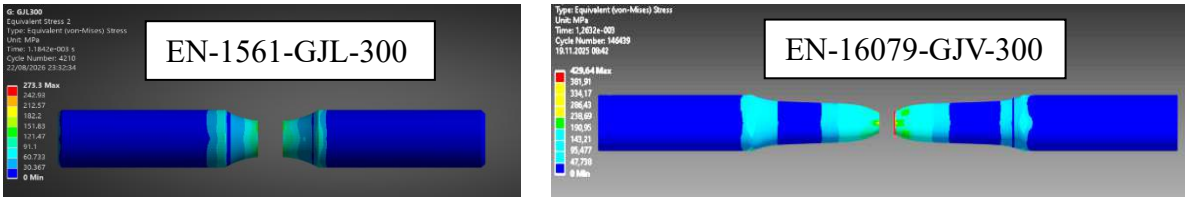
Material	Mat ID	Database/Filename	Initial Temperature (°C)
> Sand Mold		MAGMA/Coldbox_silica	20.0

[Figure 4. Compositions used in the simulations for EN-1561-GJL-300 and EN-16079-GJV-300]

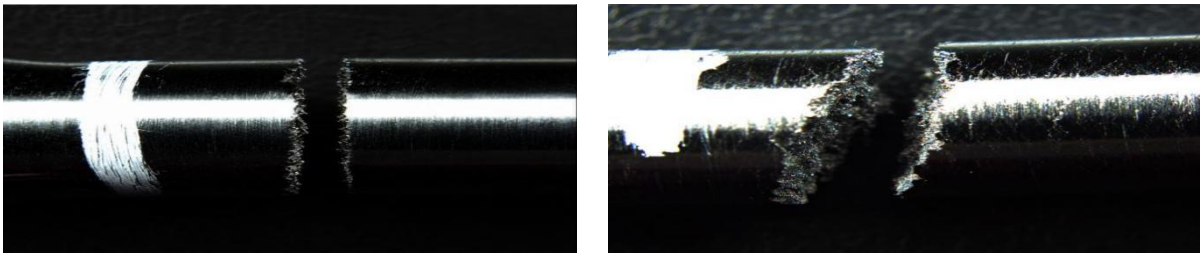
3. Results and Discussion

3.1 Mechanical Analyses

Figure 5 shows the CV-method tensile-test simulation pre- and post-test views for both materials. Table 4 compares the experimental tensile strength with the CV-method and FE-method predictions. Experimental tensile strength is lower than reference values due to inoculant method and cast model cooling/solidification effect. Brittle materials fracture without necking and produce an essentially flat fracture profile. whereas more ductile materials show measurable elongation and an uneven. off-axis fracture surface aligned with the shear plane. In the present analyses. the GJL-300 fracture profile is reproduced more faithfully by the FE simulation than the GJV-300 profile. which is consistent with the deviation values reported in Table 4: 8.2 % for GJL-300. and 6.6 % for GJV-300..



[Figure 5. CV-method tensile-test simulation images for GJL-300 and GJV-300]



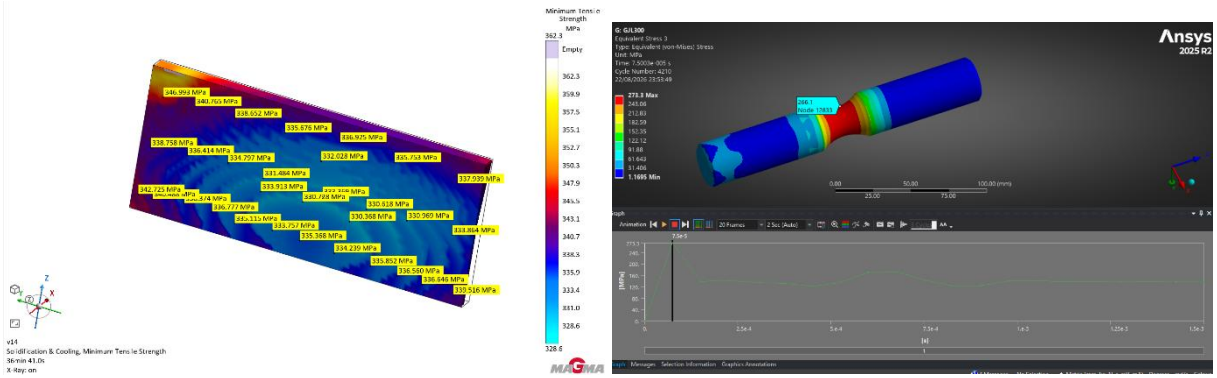
[Figure 6. Fracture-surface images of GJL-300 and GJV-300 specimens after the actual tensile test]

Table 4. Comparison of CV-method. FE-method. and experimental tensile-test results for GJL-300 and GJV-300

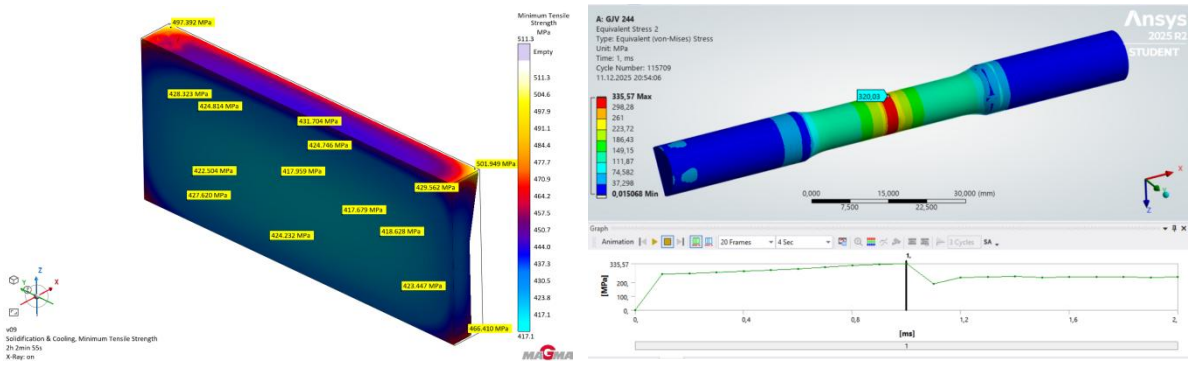
Material	CV-method simulated R_m	FE-method simulated R_m	Experimental R_m	Deviation. CV / FE
EN-GJL-300	335 MPa ±7 MPa	273 MPa	256 MPa ±14 MPa (mean ±SD, n=10)	30.9% / 6.6%
EN-GJV-300	425 MPa ±8 MPa	335 MPa	313 MPa ±7 MPa (mean ±SD, n=10)	35.8% / 7.0%

The superior agreement between the FE predictions and the experimental tensile strengths is primarily attributed to the realistic representation of the tensile-specimen geometry and loading conditions. Unlike the CV workflow, which estimates tensile strength from a section of the as-cast Y-block based mainly on solidification-derived microstructural parameters, the FE model reproduces the actual gauge section, gripping configuration, and displacement-controlled loading applied during the tensile test. Consequently, the stress distribution and failure initiation predicted by the FE model more closely resemble the experimental conditions, resulting in significantly improved prediction accuracy. In contrast, although the CV workflow exhibits lower accuracy in tensile-strength prediction, it provides complementary information on solidification behavior, graphite morphology, graphite volume fraction, and matrix-phase evolution that cannot be obtained from conventional FE analysis. In addition to estimating mechanical properties, the CV simulation predicts solidification behavior, graphite morphology, graphite volume fraction, and matrix-phase evolution. These outputs provide valuable guidance during casting-process optimization before mechanical verification by FE analysis or experimental testing. From an engineering perspective, the combined use of CV and FE simulations provides a practical workflow for cast-component development. The CV simulation enables optimization of casting parameters and prediction of microstructural evolution during process design, whereas the FE simulation provides accurate mechanical verification using the actual component or tensile-specimen geometry. Integrating both approaches can reduce development time, minimize prototype iterations, and improve confidence in material selection for engine components. Furthermore, the ability to predict local mechanical properties in geometries with high complexity ensures that the structural integrity of cast parts is maintained across varying section thicknesses[19]. Such a dual-simulation framework effectively bridges the existing gap between early-stage product development and final production by accounting for local microstructural variations that dictate macroscopic performance [20]. Future iterations of this numerical strategy may further refine accuracy by incorporating experimental microstructural data, such as phase fractions derived from image analysis, to calibrate constitutive parameters [21].

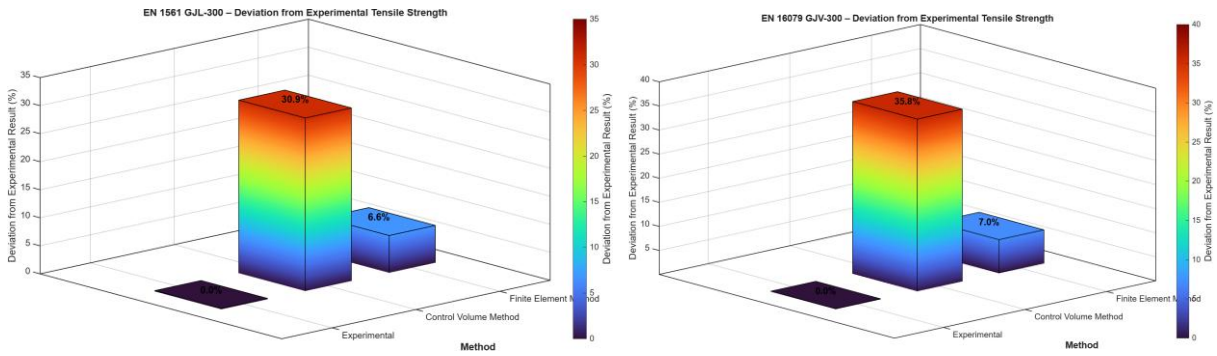
The numerical tensile strength. the fracture mode. and the von-Mises stress evolution over time for both materials are shown in Figure 7. The CV method analyses a section taken from the as-cast component geometry. whereas the FE method uses the actual tensile-specimen geometry; this is the dominant reason for the markedly smaller deviation of the FE workflow relative to experiment; the literature reports that similar geometric effects on FE tensile-test simulation accuracy have been observed as well [15].



GJL-300 Control Volume Method GJL-300 Finite Element Method



GJV-300 Control Volume Method GJV-300 Finite Element Method



[Figure 7. Comparison of CV-method. FE-method. and experimental solidification/tensile-simulation results for GJL-300 and GJV-300]

Furthermore, the FE workflow's superior performance is attributed to its integration of the Johnson–Cook constitutive model, which provides a more robust representation of the mechanical response than predictions based solely on phase-fraction evolution during solidification. Indeed, capturing the intrinsic microstructural features through FE modeling remains critical, as the material's strength at elevated temperatures significantly influences the accuracy of residual stress and deformation predictions [16].

The FE tensile-strength values are markedly closer to the experimental tensile strength than the CV-method values. The Johnson–Cook constitutive model. used in the FE workflow. is therefore a more effective representation for the tensile response of lamellar and vermicular graphite cast irons. In the CV workflow. tensile strength is predicted from a cross-section of the

standard Y-block rather than from a dedicated tension specimen. and the prediction is grounded in phase-fraction evolution during solidification.

A two-pronged numerical strategy was used to compare the microstructural and mechanical performance of EN-1561-GJL-300 and EN-16079-GJV-300: a CV-method casting-process simulation replicating the thermo-physical behaviour of solidification. and an FE-method structural analysis solving the mechanical response of the tensile specimen.

In the CV simulation, inoculation model and heat transfer coefficients are calibrated for the Y-block geometry. the furan-bonded sand mould. the 1400–1410 °C pouring temperature. the 25 °C initial mould temperature. and the experimental chemical compositions (Tables 1 and 2) were matched to experiment. The inoculation type and amount (0.15–0.25%) were defined consistent with the process records. Nodularity fraction and as-cast solidification microstructure fields were taken from the CV-method output.

In the FE simulation. the tensile-specimen geometry compliant with ISO 6892-1 was modelled as a three-dimensional digital twin and meshed at 0.5 mm (≈68.000 nodes). Boundary conditions replicated the experiment: 1 mm·min^{-1} displacement on the upper grip. fully fixed lower grip. room temperature. The Johnson–Cook elasto-viscoplastic constitutive model was used with separate parameter sets for the tensile and compressive regimes to capture the well-documented asymmetry of grey cast iron [15]. Equation 1 expresses the yield stress in terms of the reference yield stress A. the strain-hardening modulus B. the strain-hardening exponent n. the strain-rate sensitivity coefficient C. the equivalent plastic strain . the dimensionless plastic strain rate . *and the homologous temperature* }.

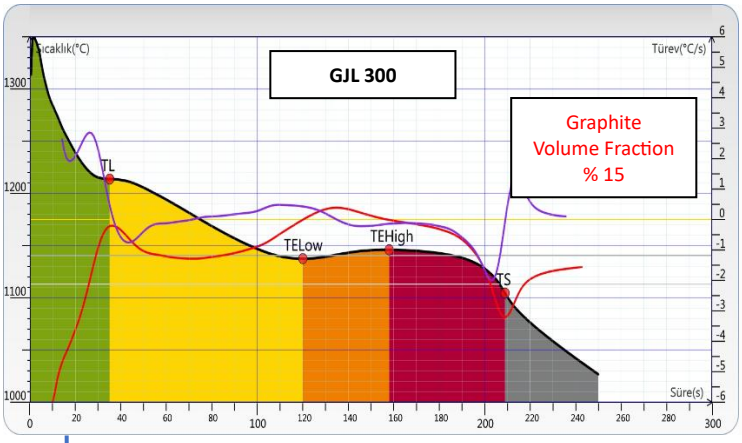
3.2 Microstructural Analyses

Figure 8 shows. for each material. as-polished (top row) and etched (middle row) optical micrographs at two magnifications. and an SEM micrograph (bottom row). Figure 9 compares the CV-method cooling curves and graphitisation-prediction outputs with the experimental graphite-phase data. The CV-method results were validated against image-analysis measurements performed on at least 15 fields of view per specimen.



[Figure 8. Optical and SEM micrographs of GJL-300 and GJV-300 at different magnifications]

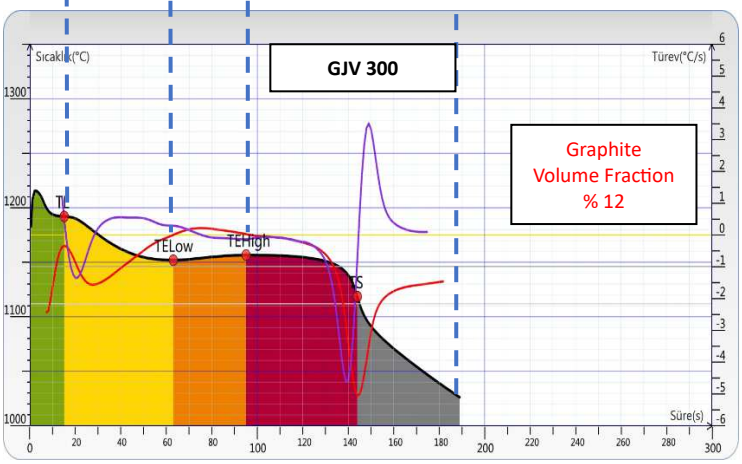
Graphite volume fraction. morphology and distribution directly determine the mechanical and thermal properties of cast irons. The presence of heterogeneous constituents degrades properties and increases the deviation between simulation and experiment.



MQ = 27 !

ACEL = 4,70

Gösterge	Min	Mevcut	Maks	Parmakizi
TL	1213,0	1212,4	1228,0	
TES	1176,0	1168,3	1187,0	
dT/dt TES	-2,00	-1,87	0,00	
S1	55,0	63,4	65,0	
TELow	1139,0	1123,3	1146,0	
R	2,0	0,0	6,0	
GRF1	60	88	90	
GRF2	15	92	45	
dT/dt TS	-4,00	-2,43	-2,50	
TS	1100,0	1073,1	1125,0	



MQ = 75 OK

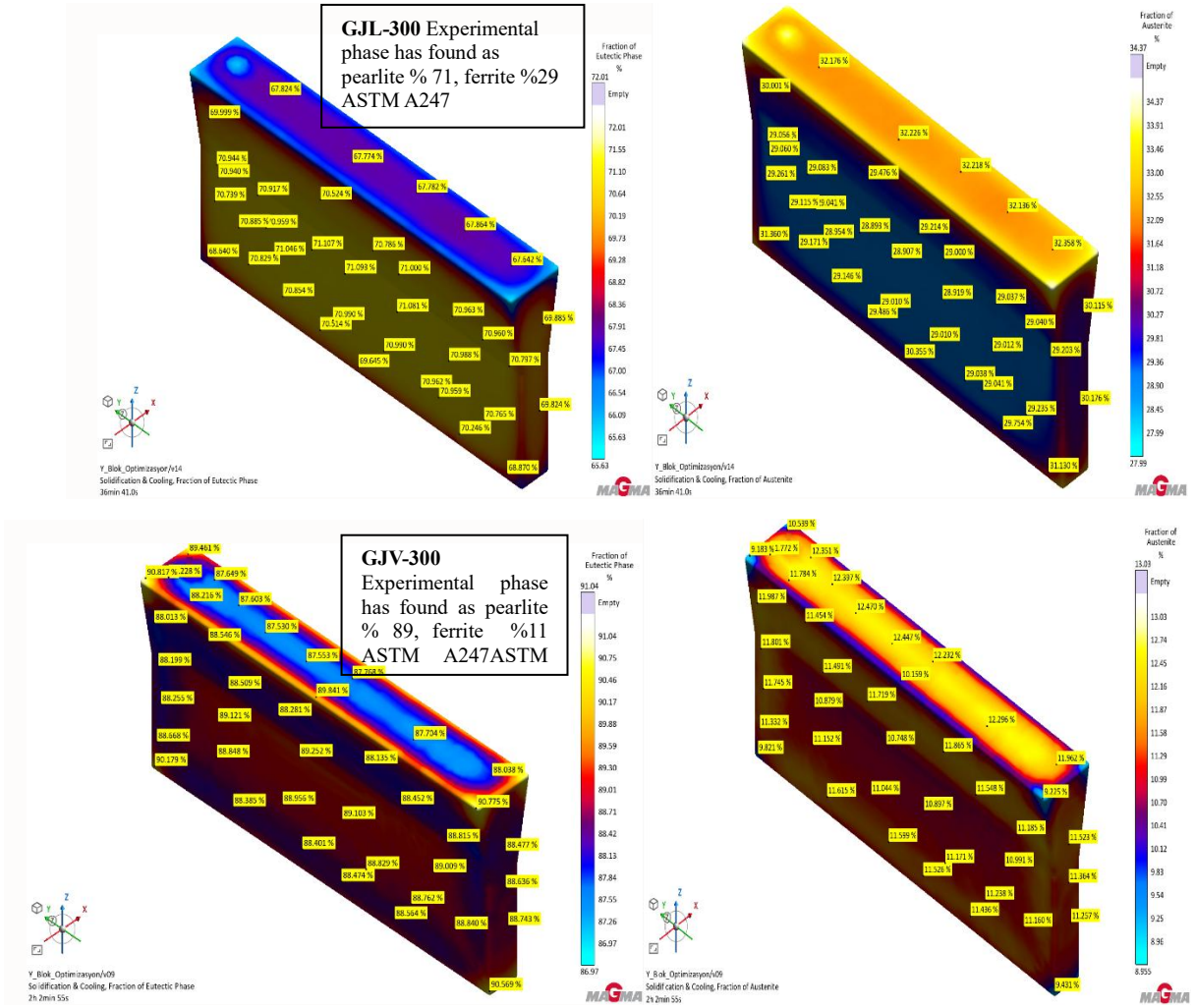
ACEL = 3,84

Gösterge	Min	Mevcut	Maks	Parmakizi
TL	1165,0	1192,1	1180,0	
TES	1154,0	1180,1	1167,0	
dT/dt TES	-2,00	-1,56	0,00	
S1	0,0	37,4	20,0	
TELow	1143,0	1151,9	1153,0	
R	2,0	4,8	10,0	
GRF1	60	71	90	
GRF2	20	17	45	
dT/dt TS	-4,00	-5,05	-2,50	
TS	1100,0	1115,7	1120,0	

[Figure 9. Comparison of CV-method cooling curves. predicted graphitisation fractions. and experimental graphite-phase data for GJL-300 (15 vol.% graphite) and GJV-300 (12 vol.% graphite)]

Inspection of the cooling curves indicates that. for GJL-300. full solidification requires approximately 250 s. with a graphitisation interval of approximately 180 s (≈88 s primary + ≈92 s secondary). For GJV-300. full solidification requires approximately 184 s. with a graphitisation interval of approximately 88 s (≈77 s primary + ≈17 s secondary). The GRF2 value in particular reflects the time required for graphite elongation rather than the graphite volume fraction itself; the elongation of lamellar graphite in the matrix requires a higher GRF2 in GJL-300. The secondary-graphitisation time of GJL-300 exceeds that of GJV-300 by a factor of approximately (92 − 17)/17 = 441%. which is consistent with the observation that the GJL-300 microstructure exhibits both higher graphite volume fraction (15 vs 12%) and longer flake length (45%). The primary-graphitisation times (88 s GJL vs 77 s GJV) correspond to a smaller but still significant relative difference.

Information on the matrix phases as a function of temperature can also be obtained from the CV-method workflow. as shown in Figure 10. The software outputs the volume fractions of the metallic phases (graphite excluded) as a function of temperature. on the basis of the equilibrium phase diagram. Eutectic and austenite phase fractions are shown separately for GJL-300 and GJV-300. Both materials are hypo-eutectic or near-eutectic; primary austenite therefore forms first. and the increase in carbon content of the remaining liquid drives eutectic-phase formation.



[Figure 10. CV-method prediction of eutectic and austenite phase volume fractions compared with experimentally measured ferrite. pearlite. and ferrite and pearlite fractions for GJL-300 (≈71% pearlite. ≈29% ferrite) and GJV-300 (≈89% pearlite. ≈11% ferrite)]

While the eutectic phase remains stable during further cooling. the austenite phase decomposes to pearlite. pearlite + ferrite. or ferrite below the eutectoid temperature of 723 °C [11]. The CV-method outputs and the room-temperature phase fractions were therefore compared on the graphite-excluded basis (100% metallic matrix). The austenite phase decomposes to ferrite. pearlite. or pearlite + ferrite depending on chemical composition and cooling rate. The GJL-300 matrix at room temperature is predominantly pearlitic (≈75–80%). The CV simulation predicts approximately 29–31% eutectic and approximately 69–71% austenite at the end of solidification; the resulting predicted room-temperature pearlite fraction is approximately 96–98%. which is significantly higher than the experimentally measured ≈71% (and ≈29% ferrite).

For GJV-300. the matrix at room temperature is also dominantly pearlitic with a small ferrite fraction (≈10–12%). Inspection of CV outputs shows approximately 10–12% retained austenite and the remainder (approximately 78–80%) as eutectic phase. Given that GJV-300 has lower concentrations of pearlite-promoting elements. the CV outputs suggest that approximately 95% of the austenite and the majority of the eutectic phase transform to ferrite. the experimentally

measured structure of GJV-300 contains approximately 89 % pearlite and approximately 11 % ferrite. consistent with the CV-method prediction within 90–92 %.

4. Conclusions

On the basis of the present comparative study of EN-1561-GJL-300 and EN-16079-GJV-300 cast irons:

1. **Tensile-strength prediction accuracy.** For both materials. the FE tensile-test simulation reproduces the experimental tensile strength with substantially smaller deviation than the CV casting-process simulation. The CV-method deviations were 30.9% for GJL-300 and 35.8% for GJV-300; the corresponding FE-method deviations were 6.6% and 7.0% respectively.
2. **Effect of geometric fidelity on prediction accuracy.** The FE workflow reduced the deviation from 35.8% to 7.0% for GJV-300 (approximately five-fold) and from 30.9% to 6.6% for GJL-300 (approximately 79%), demonstrating that improved geometric fidelity significantly reduces the discrepancy between the simulated and experimental results.
3. **Method consistency with experimental observations.** The cooling-curve and graphitisation outputs from the CV workflow are consistent with the experimental graphite volume fractions and graphite length data: longer cooling times correspond to a higher graphite volume fraction (15% GJL; 12% GJV) and longer graphite flakes (45% for GJL). The GRF1 and. particularly. GRF2 outputs are valuable indicators for predicting and tracking the length of graphite flakes and the propensity for lamellar-graphite formation.
4. **Matrix-phase prediction.** Only the CV workflow was available for matrix-phase prediction; the predicted room-temperature ferrite/pearlite ratios are in good qualitative agreement with experiment for GJV-300 at approximately 90–92% accuracy. indicating that austenite + eutectic → ferrite/pearlite transformation modelling is a useful tool. The discrepancy between predicted and measured phase fractions for GJL-300 indicates a limitation of the simple austenite-quantitative-to-pearlite assumption and warrants further work on eutectoid-transformation kinetics.
5. **Implications for engine-material selection.** Although the FE workflow gives the smaller deviation overall. the CV workflow reproduces GJL-300 tensile strength to within 15.5%—approximately 40% more accurately (in relative terms) than for GJV-300—and is the only workflow able to predict the room-temperature phase fractions. The two workflows are therefore complementary: CV for microstructural prediction at the process design stage. and FE for component-level mechanical verification.
6. **Integrated CV–FE workflow for engine-material selection.** The combined CV–FE workflow provides an efficient methodology for reducing development time, improving prediction reliability, and supporting engine-block material selection by integrating casting-process simulation, finite-element analysis, and experimental validation.

Funding

The authors received no financial support for the research, authorship, and/or publication of this article.

References

1. Stefanescu DM (2015) Science and Engineering of Casting Solidification
2. Jakubus A, Soiński MS, Mierzwa P, Stradomski G (2024) Regression Analysis and Optimum Values of Austempering Affecting Mechanical Properties of Compacted Graphite Iron. https://doi.org/10.3390/ma17205024
3. Shao S, Dawson S, Lampic M (1998) The mechanical and physical properties of Compacted Graphite Iron. https://doi.org/10.1002/mawe.19980290805
4. Cao M, Baxevanakis KP, Silberschmidt VV (2023) Effect of Graphite Morphology on the Thermomechanical Performance of Compacted Graphite Iron. https://doi.org/10.3390/met13030473
5. Luo X, Baxevanakis KP, Silberschmidt VV (2024) Crack Initiation in Compacted Graphite Iron with Random Microstructure: Effect of Volume Fraction and Distribution of Particles. https://doi.org/10.3390/ma17133346
6. Olofsson J, Svensson IL (2012) Casting and stress-strain simulations of a cast ductile iron component using microstructure based mechanical behavior. https://doi.org/10.1088/1757-899x/33/1/012051
7. Ramos AK, Diószegi A, Guesser WL, Cabezas C (2020) Microstructure of Compacted Graphite Iron Near Critical Shrinkage Areas in Cylinder Blocks. https://doi.org/10.1007/s40962-019-00403-3
8. Hahn I, Hepp E (2012) Improved ingot casting by using numerical simulation
9. Bramann H, Olofsson J, Sturm JC (2025) Probabilistic Property Modeling for Reliable Casting Design and Production. https://doi.org/10.1007/s40962-024-01535-x
10. Khan MAA, Sheikh AK (2018) Mechanical characterization and quality of iron castings using optimized mold design: simulations and experimental validation. https://doi.org/10.1007/s00170-018-2325-y
11. Brauer S, Whittington WR, Johnson K, et al (2017) Strain Rate and Stress-State Dependence of Gray Cast Iron. https://doi.org/10.1115/1.4035616
12. Sirtuli LJ, Bermejo JMB, Windmark C, et al (2024) Machining of Compacted Graphite Iron: A review. https://doi.org/10.1016/j.jmatprotec.2024.118553
13. Chen Y, Pang JC, Li SX, et al (2022) Damage mechanism and fatigue strength prediction of compacted graphite iron with different microstructures. https://doi.org/10.1016/j.ijfatigue.2022.107126
14. Salomonsson K, Olofsson J (2017) Analysis of Localized Plastic Strain in Heterogeneous Cast Iron Microstructures Using 3D Finite Element Simulations. In: The minerals, metals & materials series. Springer International Publishing, pp 217–225
15. Ozcan BF, Çalışkan U, Aydın M, et al (2025) Modeling the asymmetric thermo-mechanical behavior and failure of gray cast irons: An experimental–numerical study with separate Johnson–Cook parameters. https://doi.org/10.1016/j.simpat.2025.103182
16. Alipooramirabad H, Kianfar S, Paradowska A, Ghomashchi R (2024) Residual stress measurement in engine block—an overview. The International Journal of Advanced Manufacturing Technology 131:1–27. https://doi.org/10.1007/s00170-024-13071-3

17. Horbach L, Lyu X, Zhang J, et al (2026) Simulation-Based Assessment of Second-Order Residual Stress Fields on the Fatigue Performance of Silicon-Strengthened Ferritic Ductile Irons. Advanced Engineering Materials 28:. https://doi.org/10.1002/adem.202502518
18. Mohammadpour A, Geers MGD, Kouznetsova VG (2022) Multi-Scale Modeling of the Thermo-Mechanical Behavior of Cast Iron. Multiscale Science and Engineering 4:119–136. https://doi.org/10.1007/s42493-022-00081-0
19. Ghasemi R, Olofsson J, Jarfors AEW, Svensson IL (2016) Modelling and simulation of local mechanical properties of high silicon solution-strengthened ferritic compacted graphite iron. International Journal of Cast Metals Research 30:125–132. https://doi.org/10.1080/13640461.2016.1261520
20. Olofsson J (2014) Simulation of Microstructure-based Mechanical Behaviour of Cast Components. KTH Publication Database DiVA (KTH Royal Institute of Technology)
21. Fragassa C, Babič M, Bergmann CP, Minak G (2019) Predicting the Tensile Behaviour of Cast Alloys by a Pattern Recognition Analysis on Experimental Data. Metals 9:557–557. https://doi.org/10.3390/met9050557